Controlled Homoepitaxial Growth of Hybrid Perovskites

Yusheng Lei, Yimu Chen, Yue Gu, Chunfeng Wang, Zhenlong Huang, Haoliang Qian, Jiuyuan Nie, Geoff Hollett, Woojin Choi, Yugang Yu, NamHeon Kim, Chonghe Wang, Tianjiao Zhang, Hongjie Hu, Yunxi Zhang, Xiaoshi Li, Yang Li, Wanjun Shi, Zhaowei Liu, Michael J. Sailor, Lin Dong, Yu-Hwa Lo, Jian Luo, and Sheng Xu*

Organic–inorganic hybrid perovskites have demonstrated tremendous potential for the next-generation electronic and optoelectronic devices due to their remarkable carrier dynamics. Current studies are focusing on polycrystals, since controlled growth of device compatible single crystals is extremely challenging. Here, the first chemical epitaxial growth of single crystal $CH_3NH_3PbBr_3$ with controlled locations, morphologies, and orientations, using combined strategies of advanced microfabrication, homoepitaxy, and low temperature solution method is reported. The growth is found to follow a layer-by-layer model. A light emitting diode array, with each $CH_3NH_3PbBr_3$ crystal as a single pixel, with enhanced quantum efficiencies than its polycrystalline counterparts is demonstrated.

Y. Lei, Y. Chen, C. Wang, Dr. Z. Huang, N. Kim, C. Wang,
Y. Zhang, Y. Li, Prof. J. Luo, Prof. S. Xu
Department of Nanoengineering
University of California San Diego
La Jolla, CA 92093, USA
E-mail: shengxu@ucsd.edu

Y. Gu, J. Nie, G. Hollett, Y. Yu, T. Zhang, H. Hu, X. Li, Prof. Z. Liu,
Prof. M. J. Sailor, Prof. Y.-H. Lo, Prof. J. Luo, Prof. S. Xu
Materials Science and Engineering Program
University of California San Diego
La Jolla, CA 92093, USA

C. Wang, Prof. L. Dong
The Key Laboratory of Materials Processing and Mold
of Ministry of Education
School of Materials Science and Engineering
Zhengzhou University
Zhengzhou, Henan 450001, P. R. China

Dr. Z. Huang
School of Microelectronics and Solid State Electronics
University of Electronic Science and Technology of China
Chengdu, Sichuan 611731, P. R. China

H. Qian, W. Choi, Prof. Z. Liu, Prof. Y.-H. Lo
Department of Electrical and Computer Engineering
University of California San Diego
La Jolla, CA 92093, USA

Prof. W. Shi
Zhejiang Research Institute of Chemical Industry
Hangzhou, Zhejiang 310023, P. R. China

Prof. M. J. Sailor
Department of Chemistry and Biochemistry
University of California San Diego
La Jolla, CA 92093, USA

The ORCID identification number(s) for the author(s) of this article can be found under https://doi.org/10.1002/adma.201705992.

Organic–inorganic hybrid perovskite materials ($CH_3NH_3PbX_3$, X = Cl, Br, I) have emerged as an intriguing material system for solar cells,[1–4] photodetectors,[5–7] lasers,[8,9] and light emitting diodes (LEDs)[10–14] because of their low-temperature solution processability, tunable bandgap, and high carrier mobility.[15] However, current devices have focused on polycrystals, which suffer from high defect concentrations and therefore high free carrier recombination rates. Individual single crystal perovskite LED has been reported, but the associated fabrication process is challenging to scale up.[14] Various methods have been reported to improve the degree of crystallinity of polycrystalline perovskite thin films, including thermal annealing,[16] hot-casting,[17] and solvent engineering.[18] Notably, the photoconversion efficiency was increased from 1% to 18% by increasing the grain size from ≈1 µm to ≈180 µm.[17] Several chemical conversion strategies for synthesizing hybrid perovskites have been demonstrated,[5,10,19] but these processes generated domain boundaries and defects. Very recently, high-quality hybrid perovskite thin film with large grain sizes have been achieved from pattern substrates.[20] However, the uncontrolled grain orientation represents a barrier for single crystal thin films. On the other hand, single crystal hybrid perovskites have enhanced charge carrier transport efficiency and minimal nonradiative recombination due to low levels of trap densities, grain boundaries, and pinholes. Van der Waals (VDW) epitaxial growth on mica has been reported,[21,22] but the VDW force is much weaker than covalent bonds in conventional chemical epitaxy, and does not allow robust growth in large scale. Centimeter sized single crystals have been demonstrated with phenomenal optoelectronic properties,[23–26] but their bulky sizes do not allow integration in electronic or optoelectronic devices typically based on thin films.[25] Device integration with epitaxial growth, in a similar way to Si and III–V materials, remains a major challenge, because of the absence of a lattice matched substrate, and the material sensitivity to trace amounts of water, which precludes the use of standard lithography.[5] Here, we report a patterned homoepitaxial growth of single crystalline $CH_3NH_3PbBr_3$ (MAPbBr$_3$) at the nano/microscale with a low-temperature solution growth method. The strategy we report has a precise control over crystal position, morphology, and orientation using advanced microfabrication and homoepitaxy. The as-grown
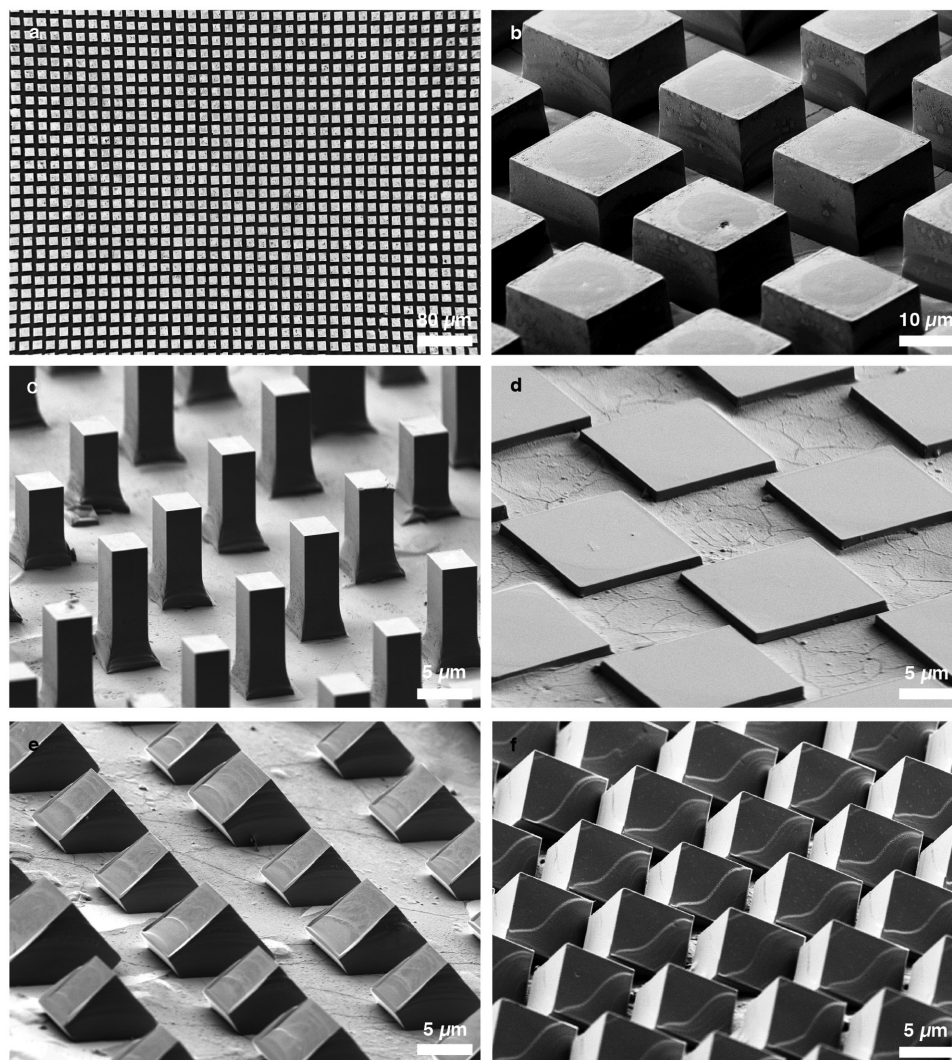
1705992 (1 of 8)

Figure 1. SEM images showing the controllable homoepitaxial growth of organic–inorganic hybrid perovskites. a) Top view of an array of epitaxial MAPbBr$_3$ single crystals and b) the corresponding tilted close-up, showing their uniform size and cubic geometry. Tilted view of crystal morphology control for c) rod and d) plate structures by controlling the crystal distribution, growth temperature, and growth time. Tilted view of crystal orientation control in e) $\langle 110 \rangle$ and f) $\langle 111 \rangle$ directions by using homoepitaxy substrates in different orientations. The crystals in (a) and (b) are grown along the $\langle 100 \rangle$ direction. All tilted view images have a tilting angle of 60°.

single crystals form a natural contact with the bottom electrode that allows facial fabrication of high performance electronic and optoelectronic devices. The high-quality materials were manifested in an array of LEDs, whose external quantum efficiency was an order of magnitude higher in comparison with their polycrystalline counterparts.

Our method uses MAPbBr$_3$ itself as a homoepitaxial substrate. On the bulk MAPbBr$_3$ single crystal substrate, we sequentially deposited Parylene-C/Cr/Au to protect it from the aqueous developer and etchant and subsequently patterned the thin films by photolithography to open sites for epitaxial growth (see the Experimental Section and Figure S1, Supporting Information). Due to its renowned hermetic properties, Parylene-C serves as a moisture protection layer as well as a strain absorption material (Figure S2, Supporting Information). Cr/Au acts as the electrode for device integration. This protocol enables robust and reproducible integration of electrodes made of

general metallic or organic materials. After cleaning the interface in an unsaturated MAPbBr$_3$ solution for several seconds, the patterned perovskite substrates were placed in a saturated MAPbBr$_3$ solution (Figure S3, Supporting Information) to grow the crystals by the inverse temperature method at different temperatures for different time durations.

Figure 1a shows the top view scanning electron microscope (SEM) image of the large-scale highly ordered epitaxial single crystalline MAPbBr$_3$ cubes grown by this method. Figure 1b shows the corresponding tilted view, indicating the uniform cubic geometry. Figures 1c,d show the tilted view SEM images of the epitaxial single crystal rods and thin plates, respectively. The crystals are uniform in size across the entire growth area on centimeter square scale. Control over the epitaxial MAPbBr$_3$ morphology is achieved by growth temperature, growth time, and pattern geometry. The growth orientation can be controlled to be $\langle 100 \rangle$ (Figures 1a–d), $\langle 110 \rangle$ (Figure 1e), and $\langle 111 \rangle$ (Figure 1f;
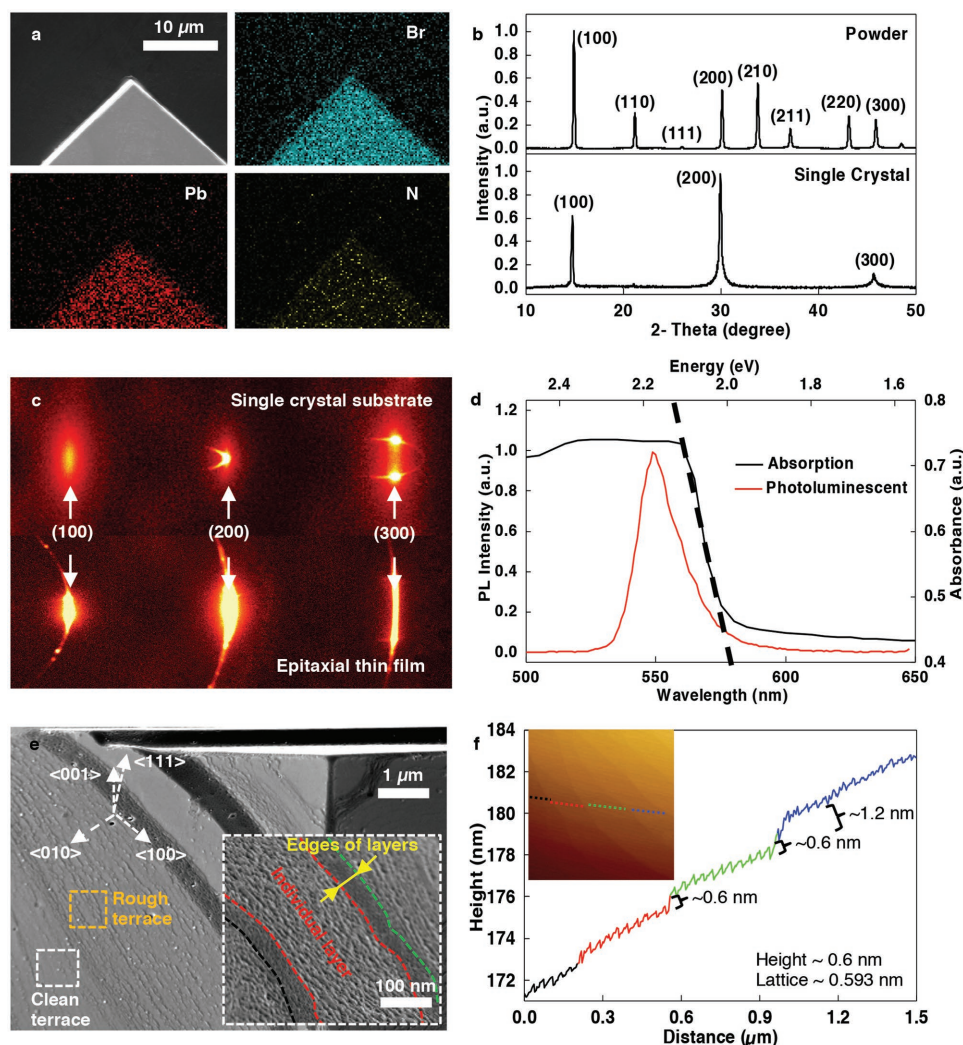
Figure 2. Structural and optical characterizations. a) EDX mapping for a typical epitaxial MAPbBr₃ single crystal. b) XRD patterns of the MAPbBr₃ powder and epitaxial thin film, confirming the *Pm3m* space group. c) 2D-XRD of the bulk crystal substrate and as-grown epitaxial crystals, both show well-aligned dominating signals, as labeled, illustrating their epitaxial relationship. d) Normalized photoluminescence and UV–vis absorption spectra for epitaxial single crystals, indicating the high crystal quality of the epitaxial single crystals. e) High magnification SEM images of surface morphology of a crystal along the ⟨111⟩ direction, showing its terrace structures. f) AFM measurement results on the surface of an epitaxial single crystal. Inset illustrates the location of the AFM scan.

Figure S4, Supporting Information) directions using different crystal planes of the MAPbBr₃ bulk crystal as the substrate (see the Supporting Information). These morphologies with different orientations provide the platform for investigating the merit of different crystal planes in electronic transport studies.[27]

Energy-dispersive X-ray spectroscopy (EDX) element mapping of the epitaxial crystals is shown in **Figure 2**a (and Figure S5, Supporting Information). The θ–2θ X-ray diffraction (XRD) spectrum shows that the epitaxial MAPbBr₃ crystals are cubic, in space group *Pm3m*, with a calculated lattice constant of 5.98 Å at room temperature (Figure 2b). 2D-XRD of the virgin substrate and the as-grown crystals with the same exposure area is shown in Figure 2c. The 2D-XRD patterns of both the substrate and the epitaxy crystals exhibit only three dominant diffraction peaks, attributed to the (100), (200), and (300) reflections of cubic MAPbBr₃, demonstrating their high degree of

crystallinity. The two sets of peaks from the substrate and epitaxial crystals show perfect alignment, indicating that the crystals have the same orientation as the substrate. The epitaxial crystals show brighter diffraction rings because the intensity is the sum of the diffraction from each individual crystal. The optical absorption spectrum of the epitaxial crystals, starting at around 575 nm, shows a clear band edge cutoff with no excitonic signatures (Figure 2d), indicating high crystal quality with minimal in-gap defect states.[23,28] The optical bandgap is calculated to be 2.16 eV. The photoluminescence (PL) spectrum of the epitaxial MAPbBr₃ shows a uniform peak at ≈550 nm with a ≈20 nm full width at half maximum without any split peaks, which confirms the high crystal quality. The narrow PL peak is shorter in wavelength than the absorption onset, implying that the PL emission can be extinguished by MAPbBr₃ itself.[25]

**ADVANCED
SCIENCE NEWS**

www.advancedsciencenews.com

**ADVANCED
MATERIALS**

www.advmat.de

To reveal the growth mechanism of the MAPbBr$_3$, we studied the surface morphology of the epitaxial single crystals (Figure 2e). An epitaxial crystal growing along the $\langle 111 \rangle$ direction is used as an example while similar phenomena are observed along the other orientations as well (Figure S6, Supporting Information). A clean and smooth terrace morphology is evident on the {100} crystal facets in high-resolution SEM images (white box in Figure 2e). The rough terrace also shows the same growth behavior (orange box in Figure 2e). The roughness is actually from tiny crystals grown when the residual solvent dries out. As shown in the inset of Figure 2e, the individual layer corresponds to one in-plane layer while the darker bands between the different colored dashed lines present edges of two different layers. This kind of trait is characteristic of the layer-by-layer growth mechanism,[29] presumably via a 2D nucleation and growth mechanism below the roughing temperature with a moderate driving force. Atomic force microscope (AFM) was used to study the terrace in high resolution, as shown in Figure 2f. The surface morphology along the scan across several terrace steps shows step heights of either 0.6 or 1.2 nm, which corresponds to integral multiples of the MAPbBr$_3$ lattice constant calculated from the XRD spectra, comparing with the negligible AFM noise level (Figure S6c, Supporting Information). Also, the observed roughness of the zig-zag curve from the AFM measurement matches the in-plane growth geometry (Figure S7, Supporting Information).

The dimethylformamide (DMF) solvent employed in our method has a high solubility of MAPbBr$_3$ (i.e., small supersaturation or driving force for the crystal growth). When the temperature slightly goes up, the deposition rate (for nucleation) overwhelms the in-plane diffusion rate (for growth) due to the large drop in solubility (i.e., large supersaturation or driving force for the crystal growth), which results in rapid nucleation at multiple sites leading to many small crystals, rather than at one single site leading to a monolithic crystal. Under the growth condition driven by room temperature evaporation in this method (see Supporting Information), the deposition rate (for nucleation) can be controlled to be extremely slow. Under this condition, we infer that the observed layer-by-layer morphology on the crystal facets is a result of the island-step-flow growth mode.[30] With a high diffusion rate and relatively low nucleation rate, interlayer transport for nucleation is suppressed and in-plane terrace diffusion for growth dominates, and most adatoms reach the in-plane edges before nucleation of new islands can occur (Figure S8, Supporting Information).

Using time-resolved photoluminescence (TRPL), we determined the carrier lifetime τ of both epitaxial single crystal and polycrystalline MAPbBr$_3$, as shown in **Figure 3**a. Epitaxial single crystals grown under 40 °C (the condition to grow high quality single crystals) were measured. Data from the polycrystalline samples were collected under the same condition. Results show that epitaxial single crystals have a fast decay lifetime of 16.39 ns
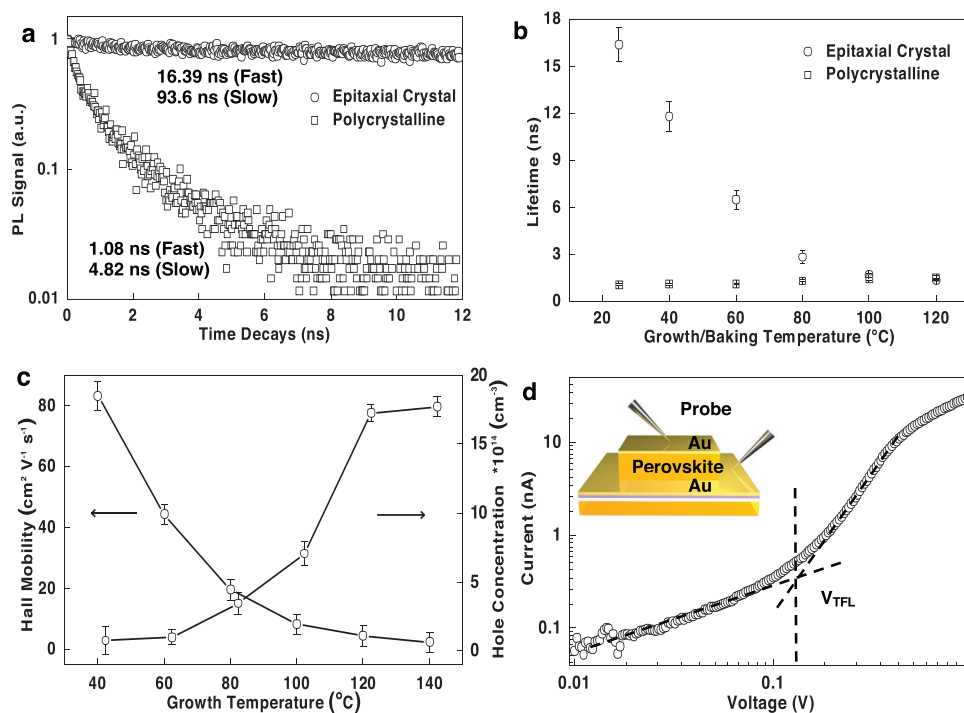

Figure 3. Electronic characterizations. a) TRPL spectra for epitaxial single crystals and a polycrystalline thin film with the same thickness of 5 µm. Both were grown at 40 °C. The epitaxial single crystals have much longer lifetimes than the polycrystalline film. b) Carrier lifetime with different growth temperatures for both epitaxial single crystal and polycrystalline film. Epitaxial single crystals grown at higher temperatures have short carrier lifetimes. The lifetime of polycrystalline thin film is relatively insensitive to the growth temperature. c) Hall effect measurement of the epitaxial MAPbBr$_3$ single crystals. The result shows p-type conduction with higher carrier mobility and lower hole concentration for crystals grown at lower temperatures. d) The I–V characteristics of the trap density measurement of the epitaxial single crystals. The inset shows the sample structure and the electrode connection scheme.

and a slow decay lifetime of 93.60 ns, which is on par with the current reported MAPbBr$_3$ bulk single crystal.[23] We assign these two very different time scales to the presence of a surface component (fast) together with a bulk component (slow), which reveals that carriers can propagate deep in the material.[23] The carrier life in epitaxial single crystals is much longer than that of the polycrystalline MAPbBr$_3$ (a fast decay lifetime of 1.08 ns and a slow decay lifetime of 4.82 ns). To illustrate the influence of growth rate on crystal quality, we studied the carrier dynamics of epitaxial MAPbBr$_3$ crystals grown at different temperatures. The results of fast decay (there is almost no slow decay in polycrystals because of the small grain size under high growth temperature) are plotted in Figure 3b (data on bulk crystals in Figure S9 of the Supporting Information also show the same trend). We found that the carrier lifetime of the epitaxial single crystal dropped significantly with fast growth rate under increased growth temperature. When the growth temperature reaches 100 °C, carrier lifetimes for epitaxial single crystal and polycrystalline MAPbBr$_3$ are almost the same. We attribute this result to the deformation of the interaction between the organic cations and the surrounding bromine halide anions under high temperatures, which can introduce a huge amount of nonradiative defects and thus significantly impair the perovskite crystal quality.[31]

Figure 3c shows the carrier mobility μ, obtained by Hall effect measurements, of the epitaxial MAPbBr$_3$ grown under different temperatures. Our MAPbBr$_3$ is found to be p-type and the hole concentration increases with increasing growth temperature. At a growth temperature of 40 °C, epitaxial single crystal MAPbBr$_3$ exhibits a carrier mobility $\mu = 82$ cm^2 V^{-1} s^{-1}. With increasing the growth temperature, the amount of defects in perovskite single crystal increases and the mobility decreases due to defect scattering.[23] To correlate these parameters with in-gap defect states, we investigated the trap density n_t using the space charge limit current method.[24] A thin layer of gold (≈25 nm) was deposited postgrowth by e-beam evaporation to form a hole-only device. Figure 3d shows the I–V characteristics measured under dark condition. Three regions can be clearly identified from the plot. At low bias (<0.12 V), the I–V shows linear ohmic response; between 0.12 to 0.50 V, a trap-filling process can be identified; above 0.50 V, the response follows a trap-filled limit regime. By calculation, we found that the epitaxial single crystal MAPbBr$_3$, with a trap filled limit voltage $V_{TFL} = 0.12$ V, has a trap density $n_t = 5.29 \times 10^{10}$ cm^{-3}, which is on par with the bulk single crystals.[23] High growth temperature leads to the increased trap density (Figure S10, Supporting Information).

Precise control of epitaxial hybrid perovskite growth on predefined sites with prepatterned electrodes allows us to fabricate high-performance functional devices. The fabrication protocol (Figure S11, Supporting Information) also applies to polymer-based hole transport layer that enables us to build an array of LEDs. **Figure 4**a shows the flat band energy-level diagram of the LED. In this structure, the MAPbBr$_3$ serves as the light emitting layer while the poly(3,4-ethylenedioxythiophene):poly(styrenesulfonate) (PEDOT:PSS) layer serves as the hole-transporting and electron-blocking layer simultaneously by virtue of its high ionization energy and low electron affinity. By controlling the growth rate, we obtained epitaxial MAPbBr$_3$ single crystals, with ≈5 μm in height and ≈20 μm by 20 μm in footprint, which

allows forming a robust contact with the bottom electrode (Figure 12, Supporting Information). A working green LED array is shown in Figure 4b. The light intensity in each crystal is uniform, which is attributed to the high crystal quality observed in our material characterizations. The color of the individual pixel is almost white dues to the high emission intensity. The electroluminescence (EL) at different voltages at room temperature is shown in Figure 4c. The intensity increases with increasing the drive voltage without any emission peak shifting, which indicates the absence of radiative decay.[32] The dominant emission peak is at around 540 nm with a full width at half maximum of about 30 nm. The integrated EL intensity under different driving voltages demonstrated a saturating tendency from 8 V with the intensity slightly decreasing at 9 and 10 V, which may be due to the inevitable heating effect at high current density levels.[10] The rapid saturation in current density in Figure 4d also demonstrated very efficient carrier injection and transport in the MAPbBr$_3$ epitaxial single crystals, further indicating that the leakage current, usually found in polycrystalline thin film-based devices,[13] is low. The turn on voltage for different devices displays some variability, with most devices having a low turn on voltage from 2 to 3 V (Figure 4e). Figure 4f shows that the maximum external quantum efficiency (EQE) of 6.1% was achieved at 9.0 V, which is an order of magnitude higher than similar devices but with polycrystalline materials.[11,33] This maximum EQE yields an internal quantum efficiency (IQE) of 28.2% considering the 21.6% transmission of the top electrode.[24] The increase in EQE with increasing applied voltage and current density suggests that a high density of charges is required for efficient radiative recombination. Future studies will focus on improvements such as optimization of the hole and electron transport layer design[12] and layer interface engineering.[16]

The strategy we reported here allows epitaxial growth of hybrid perovskite single crystals with control over their spatial distribution, morphology, and orientation. The homoepitaxy growth process follows the island-step-flow model in which the crystals are grown layer by layer when the deposition rate for nucleation is low. The epitaxial single crystals show enhanced carrier dynamics compared with polycrystalline thin films, which were manifested in single crystal LED arrays. Our study represents the first patterned epitaxial growth of perovskite single crystals—a critical advancement in device integration of organic–inorganic hybrid perovskite materials. This protocol can be applied to other materials in the hybrid perovskites family and therefore opens up new opportunities for building functional devices using these intriguing materials.

Experimental Section

Precursor Preparation: CH$_3$NH$_3$Br (MABr) was synthesized by a previously reported method.[34,35] First, hydrobromic acid (15.6 mL, 48 wt% in water, Aldrich) was mixed with methylamine (20 mL, 40% in methanol, Tokyo Chemical Industry Co.) in ice-water bath and stirred for 2 h in a flask. After that, the flask was placed onto a hot plate at 50 °C with stirring to remove the solvent. The reaction product, MABr was washed with ethanol by stirring the mixture for 30 min. The precipitate was then centrifuged for three times with anhydrous diethyl ether and dried under 80 °C in convection oven for overnight. The derived MABr was in the form of white powder.
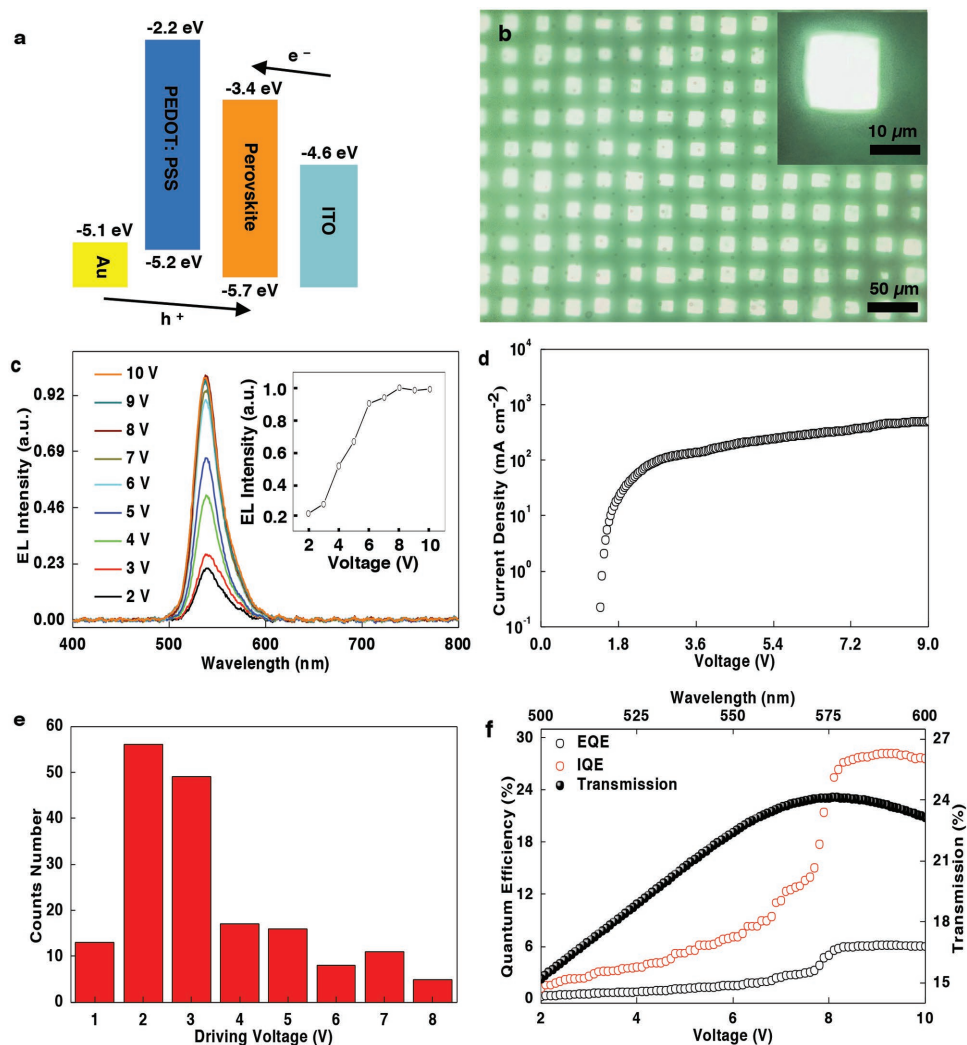
Figure 4. Device demonstration. a) The flat band energy-level diagram of the fabricated LEDs. b) Optical images of a working LED array, showing uniform and high-intensity light emission from individual single crystals. c) Normalized EL intensity as a function of the drive voltage. The emission peak does not shift, showing that the recombination region does not change under different drive voltages. The EL intensity saturates at around 8 V (inset). d) Current density of a working LED array under different driving voltages. The rapid saturation reveals a minimal leakage current due to the high quality of single crystals. e) Summary of turn on voltages needed to light up the epitaxial single crystal LEDs. f) EQE, transmission, and IQE of the epitaxial single crystal LED array. An EQE of 6.1% is achieved at 9.0 V.

Crystal Preparation: MABr precursor (0.748 g) prepared as above was dissolved in anhydrous DMF (4 mL, 99.8%, Aldrich) in a 20 mL glass vial to form a clear solution. Then, $PbBr_2$ (2.452 g, 98%, Alfa Aesar) was added into the glass vial with stirring to get nearly saturated clear $MAPbBr_3$ solution. The glass vial was placed onto a hot plate at 25–35 °C without disturbance for slow evaporation. Bulk $MAPbBr_3$ single crystals with dimensions in the centimeter range could be obtained from the solution after 24 h.

Mechanical Polishing: A piece of 1200 grid sand paper was used to polish the large cubic crystal to get perovskite substrate with thin thickness or different facets. During the polishing process, anhydrous 2-propanol (IPA) (99.5%, Aldrich) was used to continuously wash away the grinded perovskite powder, which would otherwise scratch the polished surface. To obtain different facets, the bulk crystal was precisely fixed in a thick layer of uncured polydimethylsiloxane (PDMS) precursor (Sylgard 184 silicone elastomer, 20:1, Aldrich) with the target orientation facing perpendicular to the PDMS surface, then the mold was placed on a hot plate at 70 °C for 10 min to cure. Then, the mold was used to do

the polishing on a sand paper with continuous anhydrous IPA washing to expose different facets.

Lithography: The $CH_3NH_3PbBr_3$ substrate was coated with a layer of Parylene-C (≈500 nm in thickness) to form an overall moisture resistant and strain absorption layer. It was then sputtered with Cr (≈50 nm in thickness) and Au (≈100 nm in thickness) sequentially as the adhesion and electrode layers. After this, photoresist (AZ-1512) was spin-coated onto the $MAPbBr_3$ substrate for photolithography. Then, the Au and Cr were etched sequentially (Au was chemically etched by Au etchant while Cr was etched by reactive ion etching). The residual photoresist was then washed by acetone (99.5%, Aldrich) followed by Parylene-C dry etching to get the patterned $MAPbBr_3$ substrate.

Solution Growth: The patterned $MAPbBr_3$ substrate was placed in an nearly-saturated $MAPbBr_3$ DMF solution (0.748 g MABr precursor, 2.452 g $PbBr_2$, and 4 mL anhydrous DMF) for 30 s to remove the polycrystalline layer on the patterned surface caused by O_2 plasma etching.[36] Then, the $MAPbBr_3$ substrate was put into a room-temperature saturated $MAPbBr_3$ DMF solution with a Teflon scaffold to hold the substrate facing down,

to avoid incidental precipitation onto the substrate during heating up, which would otherwise interfere with the normal crystal growth. The vial was placed onto a hot plate to grow the epitaxial perovskite single crystals from the patterned openings under different temperatures. It is worth noting that different growth temperatures and different sizes of the patterned openings could result in different morphologies of the epitaxial perovskite crystals: high temperature (>80 °C) with small holes (<5 µm) could result in rod-like structure; low temperature (<60 °C) with large holes (>10 µm) could lead to plate-like structure; low temperature (<60°C) and medium sized holes (5–10 µm) could generate cubic-like structure. Growth in other orientations, such as in ⟨110⟩ and ⟨111⟩, also shows the same tendency.

Device Fabrication: The polished MAPbBr$_3$ substrate was coated with a layer of Parylene-C (≈500 nm in thickness) followed by sputtering of layers of Cr (≈50 nm in thickness) and Au (≈100 nm in thickness). 0.5 mL PEDOT:PSS (Aldrich) was mixed with 10 mL anhydrous IPA, and the mixture was treated under ultrasound for 30 min to ensure homogeneous dissolution. After this, a layer of PEDOT:PSS (≈200 nm in thickness) was deposited onto the Au layer using a spray gun, with the substrate on a hot plate at 80 °C to instantaneously evaporate the solvent. Then, sequential deposition of layers of Parylene-C, poly(methyl methacrylate) (PMMA), and SiO$_2$ on top of the PEDOT:PSS was made to assist patterning of PEDOT:PSS. The thickness of each layer would not affect the fabrication process as they were sacrificial materials to be removed. Specially, the Parylene-C layer on the PEDOT:PSS helped fix the PEDOT:PSS layer during the Au wet etching process to avoid the loss of PEDOT:PSS; the spin-coated PMMA helped increase the adhesion between Parylene-C and SiO$_2$; the SiO$_2$ layer played as a top patterning and etch stop layer. After this, photoresist was spin-coated onto the SiO$_2$ layer for photolithography. In the etching process, SiO$_2$, Parylene-C, PMMA, PEDOT:PSS, and Cr were removed by dry etching; Au was removed by wet etching. Then the patterned perovskite/Parylene-C/Cr/Au/PEDOT:PSS structure was obtained. Based on this structure, epitaxial perovskite single crystals were grown from solution. After growing the epitaxial crystal arrays (≈5 µm in thickness), photoresist was spin-coated on the epitaxial single crystal arrays to form an insulation layer. Slight etching of the insulation layer would expose the top portion of the epitaxial crystal array, while the bottom portion and the bottom substrate were still insulated by the photoresist layer. A layer of indium tin oxide (≈200 nm in thickness) was deposited by sputtering to form the top electrode of the final LEDs (Figure S11, Supporting Information).

Material Characterizations: The as-grown crystals were inspected using a Zeiss Sigma 500 SEM. The PL spectra and TRPL of epitaxial perovskite crystals were measured by Microscope Olympus IX81 with a MaiTai HP laser in a black box at room temperature. Powder XRD and single crystal 2D XRD were measured using a state-of-the-art Bruker Single-Crystal Diffractometer and a Bruker Bulk Diffractometer with Cu Kα (λ = 1.5406 Å) radiation, respectively. CH$_3$NH$_3$PbBr$_3$ powders were made by grinding a large piece of crystal into fine powders in a mortar. EDX mapping was preformed through the field emission environmental SEM (FEI/Phillips XL30 ESEM). Absorption and transmittance spectra were collected with a Perkin Elmer Lambda 1050 UV–Vis with an internally coupled integrating sphere. To measure their absorption spectra, the epitaxial single crystals were grown and peeled off from a bulk perovskite substrate. For the crystal surface investigation, the morphology of the perovskite epitaxial crystals was determined using the AFM (Veeco Scanning Probe Microscope) under tapping mode. AFM measurement was carried out on crystals grown with different conditions. All of the results showed the same phenomenon. Trap density was characterized and calculated through the reported *I–V* measurement (SCLC) method[23,24,26] with a home-built probe station that included a black box and a Keithley 2400 source meter under dark environment and room temperature. The top and bottom Au layers were deposited by e-beam evaporation. Hall effect was measured using Lake Shore Hall measurement system (HM 3000) with the four contacts van der Pauw method.[25] To use e-beam evaporation to deposit the four Au contacts onto the epitaxial crystals, Parylene-C served as the only mask material (to avoid the influence of metals) to grow continuous

epitaxial single crystal thin films. All samples were measured at room temperature.

LED Characterizations: All LED devices were connected through two Cu wires to external equipment for the following characterizations. EL characteristics were measured using a Keithley 2400 source meter with an Ocean Optics QE65 Pro TE-cooled CCD spectrophotometer under dark environment. Current density measurements were performed with the same setup used in trap density measurements under the same conditions. The EQE of the device was measured using a home-built measurement system, which included a source meter, an integration sphere, and an optical power meter (1936-R, Newport). All of the optical images were taken by a Zeiss Axio Imager Optical Microscope.

Supporting Information

Supporting Information is available from the Wiley Online Library or from the author.

Acknowledgements

Conflict of Interest

The authors declare no conflict of interest.

Keywords

[1] A. Kojima, K. Teshima, Y. Shirai, T. Miyasaka, *J. Am. Chem. Soc.* **2009**, *131*, 6050.

[2] M. Liu, M. B. Johnston, H. J. Snaith, *Nature* **2013**, *501*, 395.

[3] N. J. Jeon, J. H. Noh, Y. C. Kim, W. S. Yang, S. Ryu, S. I. Seok, *Nature* **2015**, *517*, 476.

[4] J. M. Ball, M. M. Lee, A. Hey, H. J. Snaith, *Energy Environ. Sci.* **2013**, *6*, 1739.

[5] G. Wang, D. Li, H. C. Cheng, Y. Li, C. Y. Chen, A. Yin, Z. Zhao, Z. Lin, H. Wu, Q. He, M. Ding, *Sci. Adv.* **2015**, *1*, e1500613.

[6] L. Dou, Y. M. Yang, J. You, Z. Hong, W. H. Chang, G. Li, Y. Yang, *Nat. Commun.* **2014**, *5*, 5404.

[7] Y. Lee, J. Kwon, E. Hwang, C. H. Ra, W. J. Yoo, J. H. Ahn, J. H. Park, J. H. Cho, *Adv. Mater.* **2015**, *27*, 41.

[8] Q. Zhang, S. T. Ha, X. Liu, T. C. Sum, Q. Xiong, *Nano Lett.* **2014**, *14*, 5995.

**ADVANCED
SCIENCE NEWS**

www.advancedsciencenews.com

**ADVANCED
MATERIALS**

www.advmat.de

[9] H. Zhu, Y. Fu, F. Meng, X. Wu, Z. Gong, Q. Ding, M. V. Gustafsson, M. T. Trinh, S. Jin, X. Y. Zhu, *Nat. Mater.* **2015**, *14*, 636.

[10] A. B. Wong, M. Lai, S.W. Eaton, Y. Yu, E. Lin, L. Dou, A. Fu, P. Yang, *Nano Lett.* **2015**, *15*, 5519.

[11] Z. F. Shi, X. G. Sun, D. Wu, T. T. Xu, S. W. Zhuang, Y. T. Tian, X. J. Li, G. T. Du, *Nanoscale* **2016**, *8*, 10035.

[12] Z. K. Tan, R. S. Moghaddam, M. L. Lai, P. Docampo, R. Higler, F. Deschler, M. Price, A. Sadhanala, L. M. Pazos, D. Credgington, F. Hanusch, *Nat. Nanotechnol.* **2014**, *9*, 687.

[13] Z. Xiao, R. A. Kerner, L. Zhao, N. L. Tran, K. M. Lee, T. W. Koh, G. D. Scholes, B. P. Rand, *Nat. Photonics* **2017**, *11*, 108.

[14] M. Chen, X. Shan, T. Geske, J. Li, Z. Yu, *ACS Nano* **2017**, *11*, 6312.

[15] J. Huang, Y. Yuan, Y. Shao, Y. Yan, *Nat. Rev. Mater.* **2017**, *2*, 17042.

[16] H. Zhou, Q. Chen, G. Li, S. Luo, T. B. Song, H. S. Duan, Z. Hong, J. You, Y. Liu, Y. Yang, *Science* **2014**, *345*, 542.

[17] W. Nie, H. Tsai, R. Asadpour, J. C. Blancon, A. J. Neukirch, G. Gupta, J. J. Crochet, M. Chhowalla, S. Tretiak, M. A. Alam, H. L. Wang, A. D. Mohite, *Science* **2014**, *347*, 522.

[18] N. J. Jeon, J. H. Noh, Y. C. Kim, W. S. Yang, S. Ryu, S. I. Seok, *Nat. Mater.* **2014**, *13*, 897.

[19] J. A. Koza, J. C. Hill, A. C. Demster, J. A. Switzer, *Chem. Mater.* **2015**, *28*, 399.

[20] T. Geske, J. Li, M. Worden, X. Shan, M. Chen, S. G. R. Bade, Z. Yu, *Adv. Funct. Mater.* **2017**, *27*, 1702180.

[21] Y. Wang, Y. Shi, G. Xin, J. Lian, J. Shi, *Cryst. Growth Des.* **2014**, *15*, 4741.

[22] S. T. Ha, X. Liu, Q. Zhang, D. Giovanni, T. C. Sum, Q. Xiong, *Adv. Opt. Mater.* **2014**, *2*, 838.

[23] D. Shi, V. Adinolfi, R. Comin, M. Yuan, E. Alarousu, A. Buin, Y. Chen, S. Hoogland, A. Rothenberger, K. Katsiev, Y. Losovyj, X. Zhang, P. A. Bowben, O. F. Mohammed, E. H. Sargent, O. M. Bakr, *Science* **2014**, *347*, 519.

[24] Q. Dong, Y. Fang, Y. Shao, P. Mulligan, J. Qiu, L. Cao, J. Huang, *Science* **2015**, *347*, 967.

[25] Y. Liu, Z. Yang, D. Cui, X. Ren, J. Sun, X. Liu, J. Zhang, Q. Wei, H. Fan, F. Yu, X. Zhang, C. Zhao, S. Liu, *Adv. Mater.* **2015**, *27*, 5176.

[26] M. I. Saidaminov, A. L. Abdelhady, B. Murali, E. Alarousu, V. M. Burlakov, W. Peng, I. Dursun, L. Wang, Y. He, G. Maculan, A. Goriely, T. Wu, O. F. Mohammed, M. Bakr, *Nat. Commun.* **2015**, *6*, 7586.

[27] S. Y. Leblebici, L. Leppert, Y. Li, S. E. Reyes-Lillo, S. Wickenburg, E. Wong, J. Lee, M. Melli, D. Ziegler, D. K. Angell, D. F. Ogletree, *Nat. Energy* **2014**, *1*, 16093.

[28] Y. Chen, Q. Ge, Y. Shi, J. Liu, D. Xue, J. Ma, J. Ding, H. Yan, J. Hu, L. Wan, *J. Am. Chem. Soc.* **2016**, *138*, 16196.

[29] M. Kawasaki, K. Takahashi, T. Maeda, R. Tsuchiya, *Science* **1994**, *266*, 1540.

[30] K. W. Kolasinski, *Surface Science: Foundations of Catalysis and Nano-science*, Wiley, Hoboken, NJ, USA **2012**.

[31] S. D. Stranks, H. J. Snaith, *Nat. Nanotechnol.* **2015**, *10*, 391.

[32] J. Kalinowski, *Organic Light-Emitting Diodes: Principles, Characteristics, and Processes*, Marcel Dekker, New York, NY, USA **2005**.

[33] Y. Ling, Z. Yuan, Y. Tian, X. Wang, J. Wang, Y. Xin, K. Hanson, B. Ma, H. Gao, *Adv. Mater.* **2016**, *28*, 305.

[34] A. Dymshits, A. Rotem, L. Etgar, *J. Mater. Chem. A* **2014**, *2*, 20776.

[35] S. Aharon, B. E. Cohen, L. Etgar, *J. Phys. Chem. C* **2014**, *118*, 17160.

[36] S. Yuan, Z. Qiu, H. Zhang, H. Gong, Y. Hao, B. Cao, *Appl. Phys. Lett.* **2016**, *108*, 033904.